

## Supporting Information

### **Preparation of Lactic Acid- and Glucose-Responsive Poly( $\epsilon$ -caprolactone)-*b*-Poly(ethylene oxide) Block Copolymer Micelles Using Phenylboronic Ester as a Sensitive Block Linkage**

David Vrbata, Mariusz Uchman\*

*Department of Physical and Macromolecular Chemistry, Faculty of Science, Charles  
University, Hlavova 2030, 128 40 Prague 2, Czech Republic*

*\*e-mail: uchman@natur.cuni.cz*

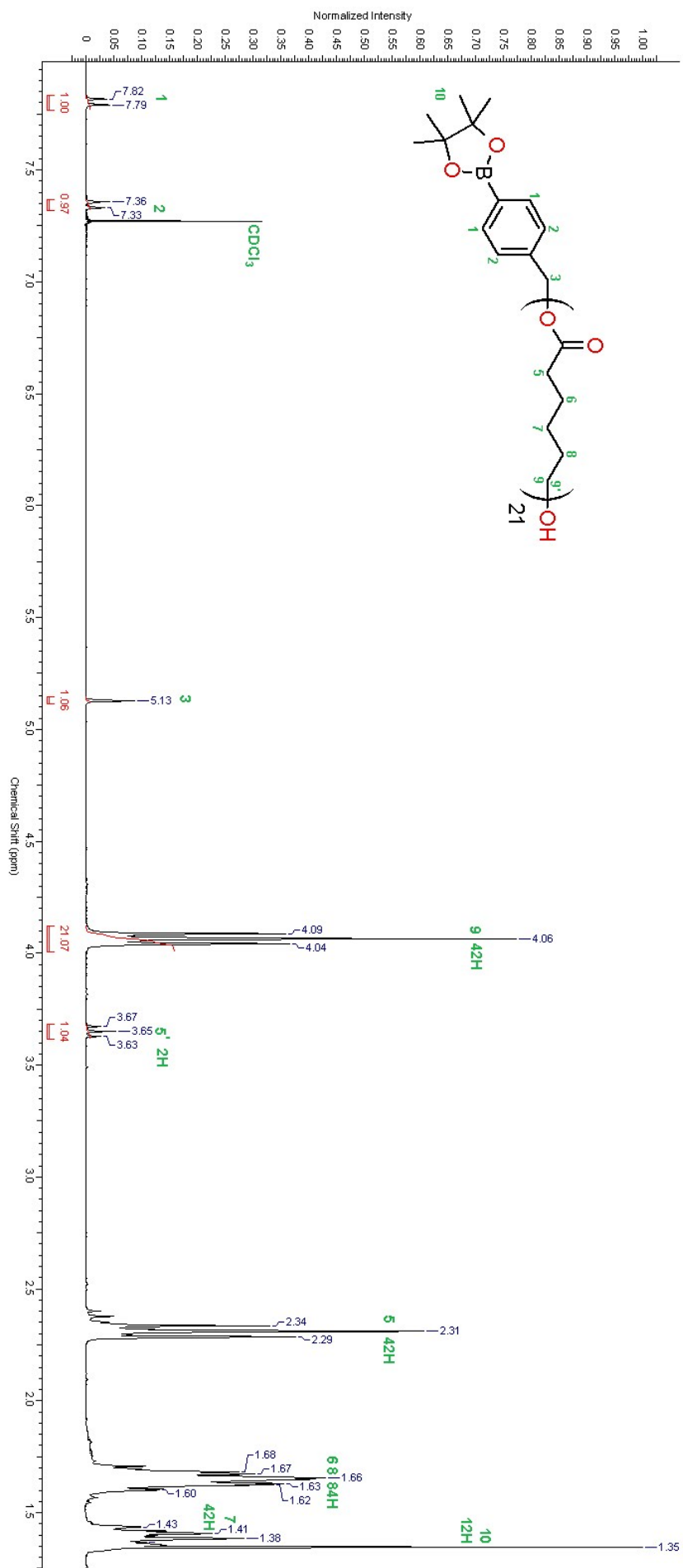


**Figure S1.** <sup>1</sup>H NMR spectra of  $\alpha$ -(((4,4,5,5-tetramethyl-1,3,2-dioxaborolan-2-yl)benzyl)oxy)polycaprolactone

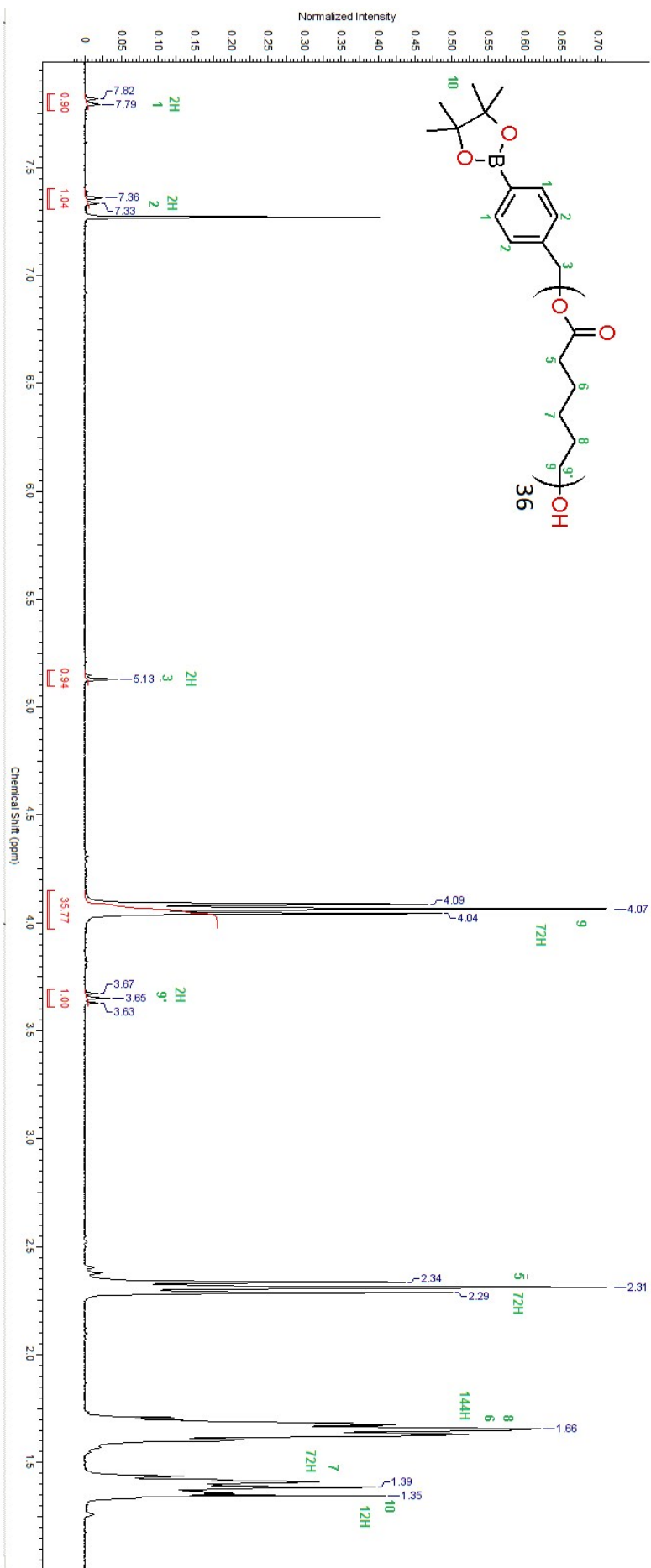


**Figure S2.** <sup>1</sup>H NMR spectra of α-(((4,4,5,5-tetramethyl-1,3,2-dioxaborolan-2-yl)benzyl)oxy)polycaprolactone

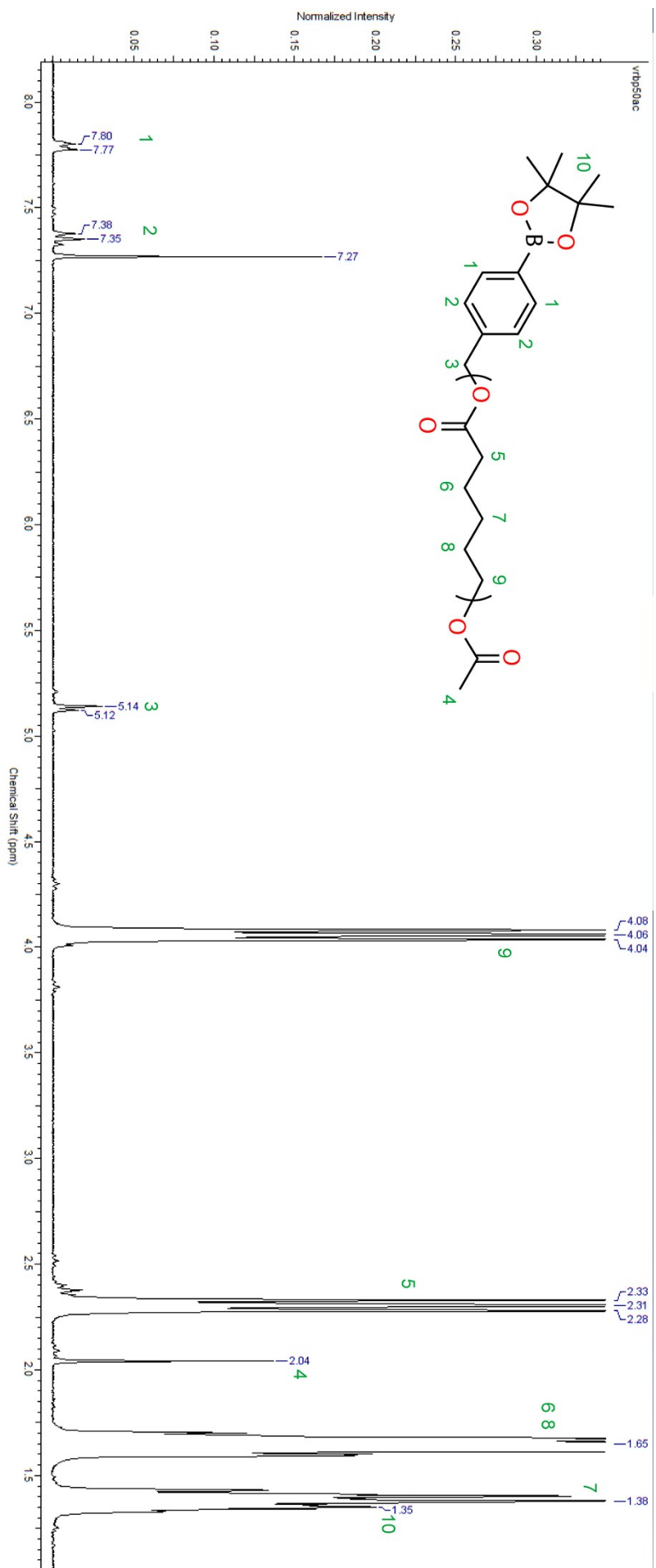


**Figure S3.** <sup>1</sup>H NMR spectra of α-(((4,4,5,5-tetramethyl-1,3,2-dioxaborolan-2-yl)benzyl)oxy)-ω-acetyl polycaprolactone

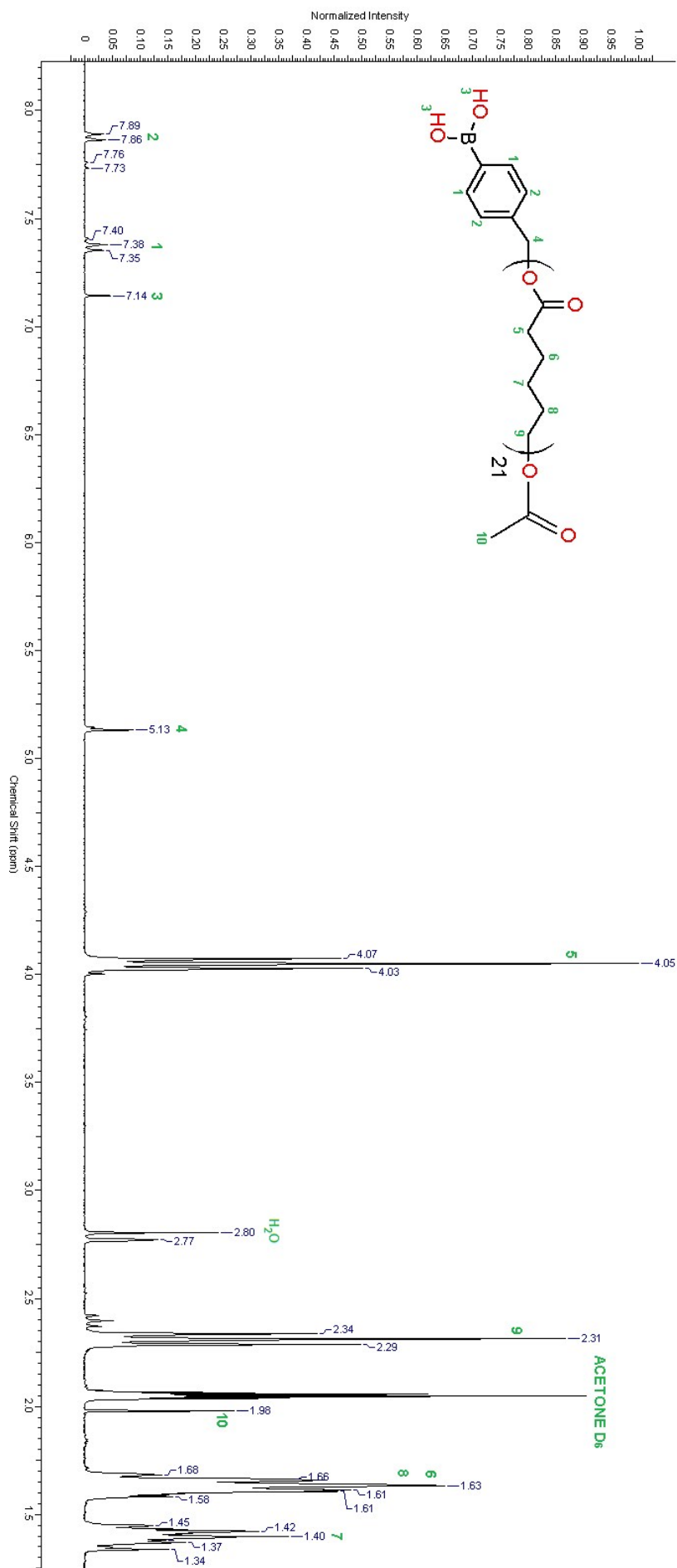


Figure S4. <sup>1</sup>H NMR spectra of  $\alpha$ -((4-boronobenzyl)oxy)- $\omega$ -acetyl polycaprolactone

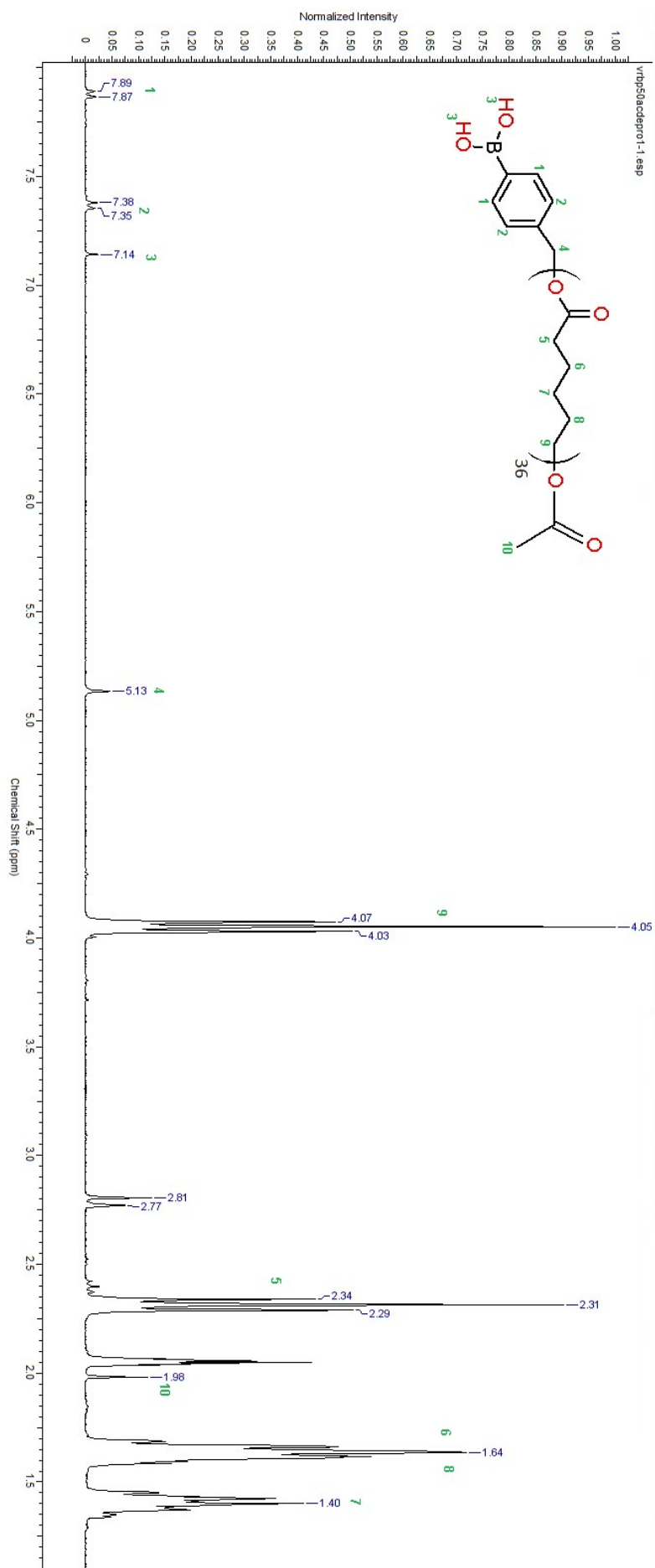


Figure S5.  $^1\text{H}$  NMR spectra of  $\alpha$ -((4-boronobenzyl)oxy)- $\omega$ -acetyl polycaprolactone

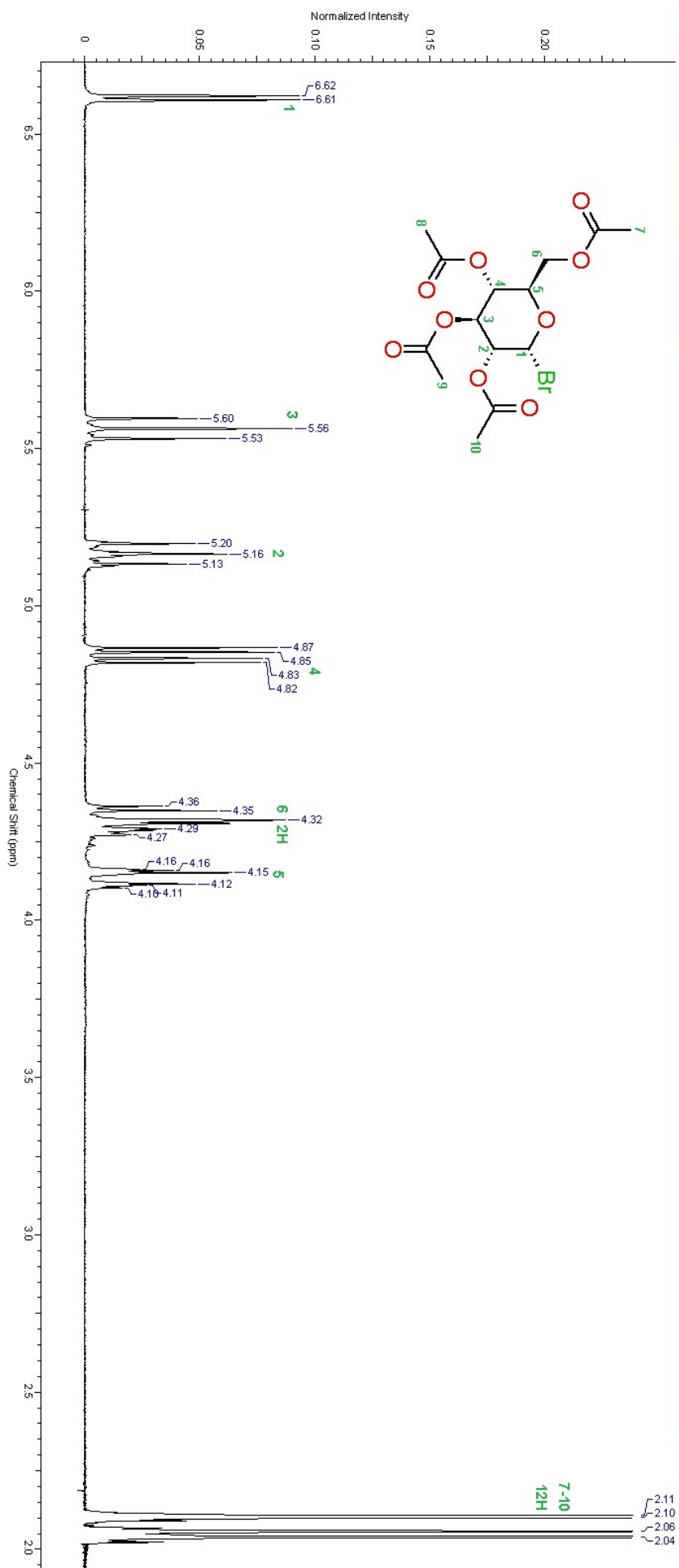


Figure S6.  $^1\text{H}$  NMR spectra of 1-bromo-2,3,4,6-tetra-O-acetyl-D-glucopyranoside

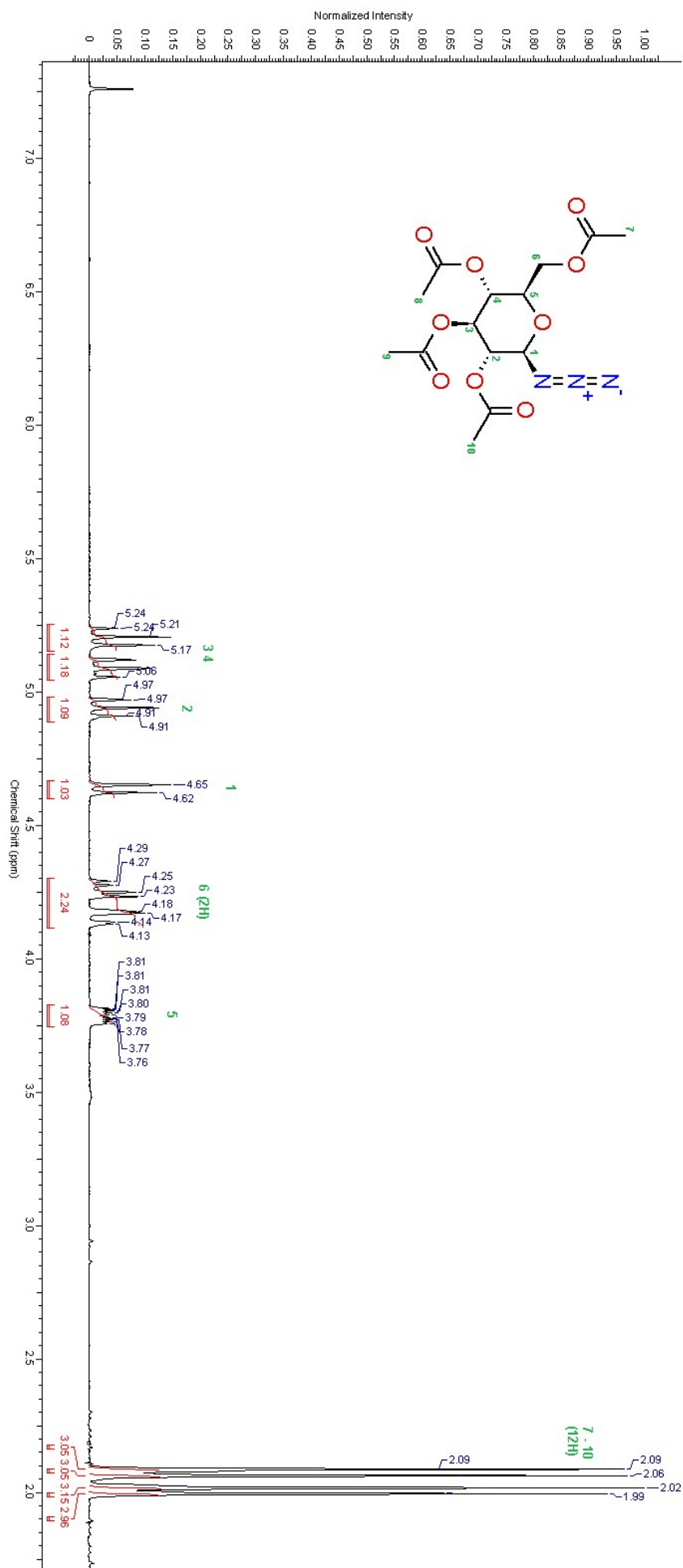


Figure S7.  $^1\text{H}$  NMR spectra of 1-azido-2,3,4,6-tetra-O-acetyl-D-glucopyranoside

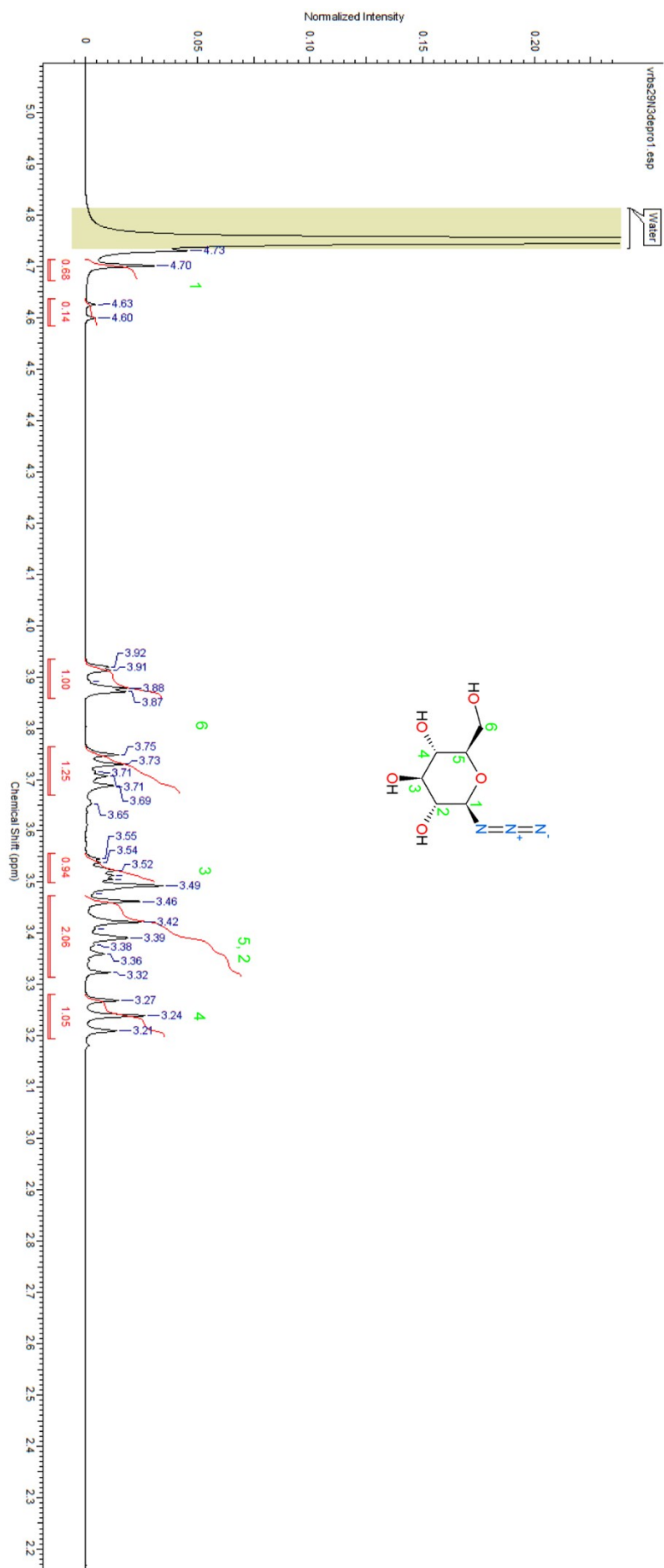


Figure S8.  $^1\text{H}$  NMR spectra of 1-azido-2,3,4,6-tetra-O-acetyl-D-glucopyranoside

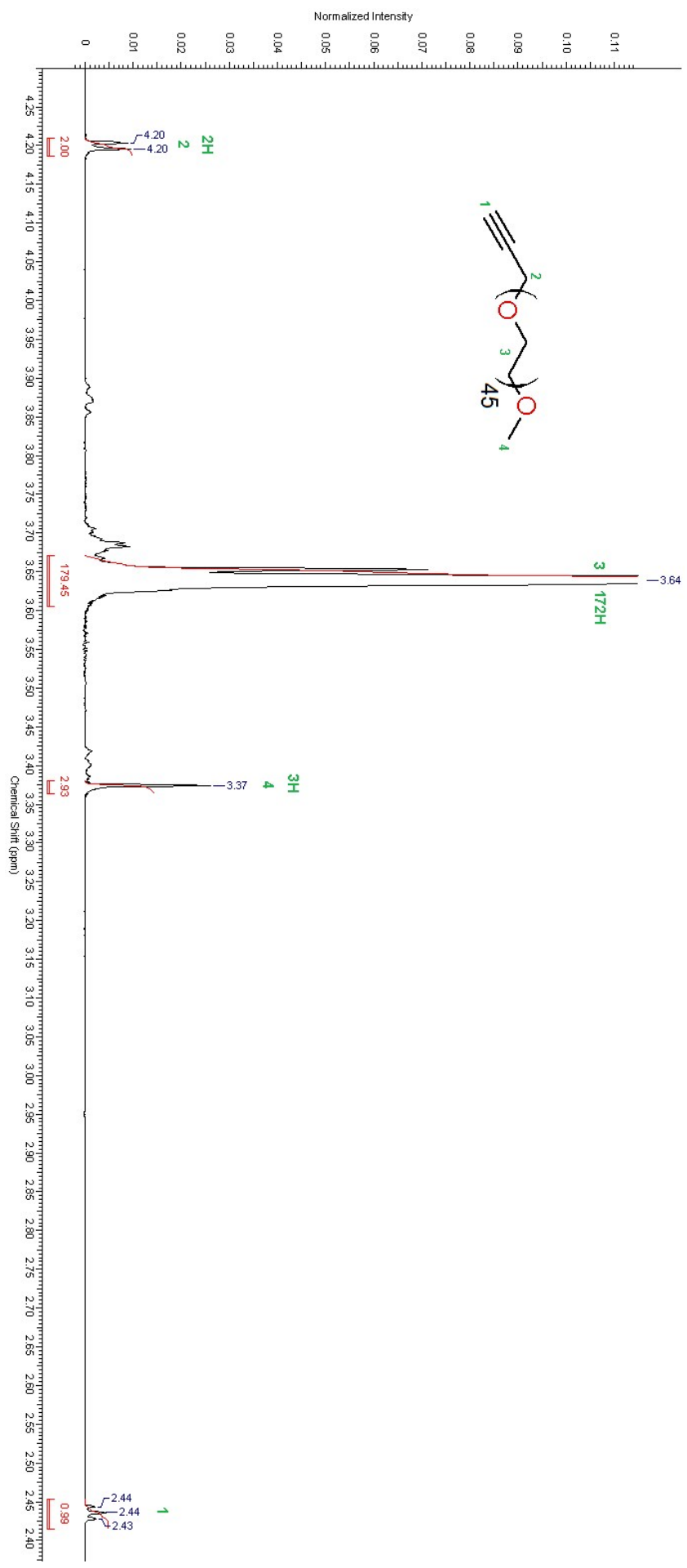
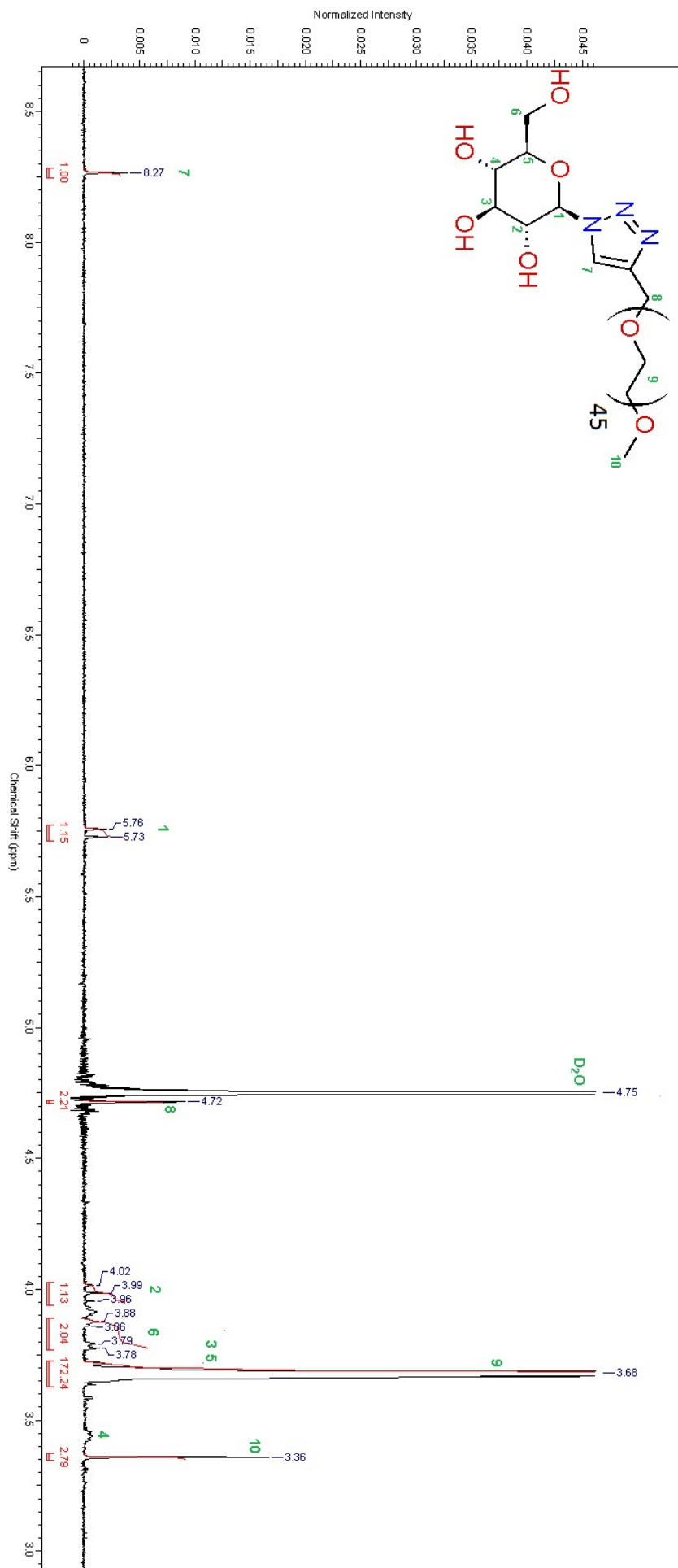
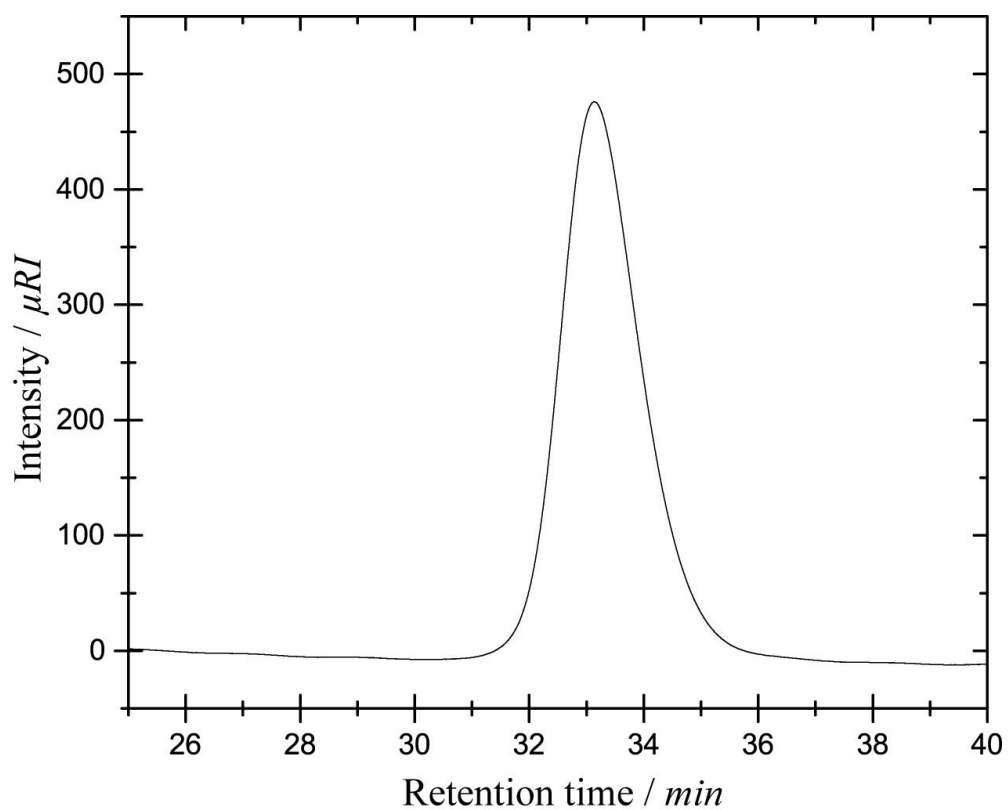


Figure S9. <sup>1</sup>H NMR spectra of α-methoxy-ω-propargylpoly(ethylene oxide)



**Figure S10.**  $^1\text{H}$  NMR spectra of  $\alpha$ -((1-deoxy- $\alpha$ ,D-glucopyranos-2-yl)-1H-1,2,3-triazol-4-yl)- $\omega$ -methoxy poly(ethylene oxide)



**Figure S11.** SEC traces of  $\alpha$ -(((4,4,5,5-tetramethyl-1,3,2-dioxaborolan-2-yl)benzyl)oxy)polycaprolactone

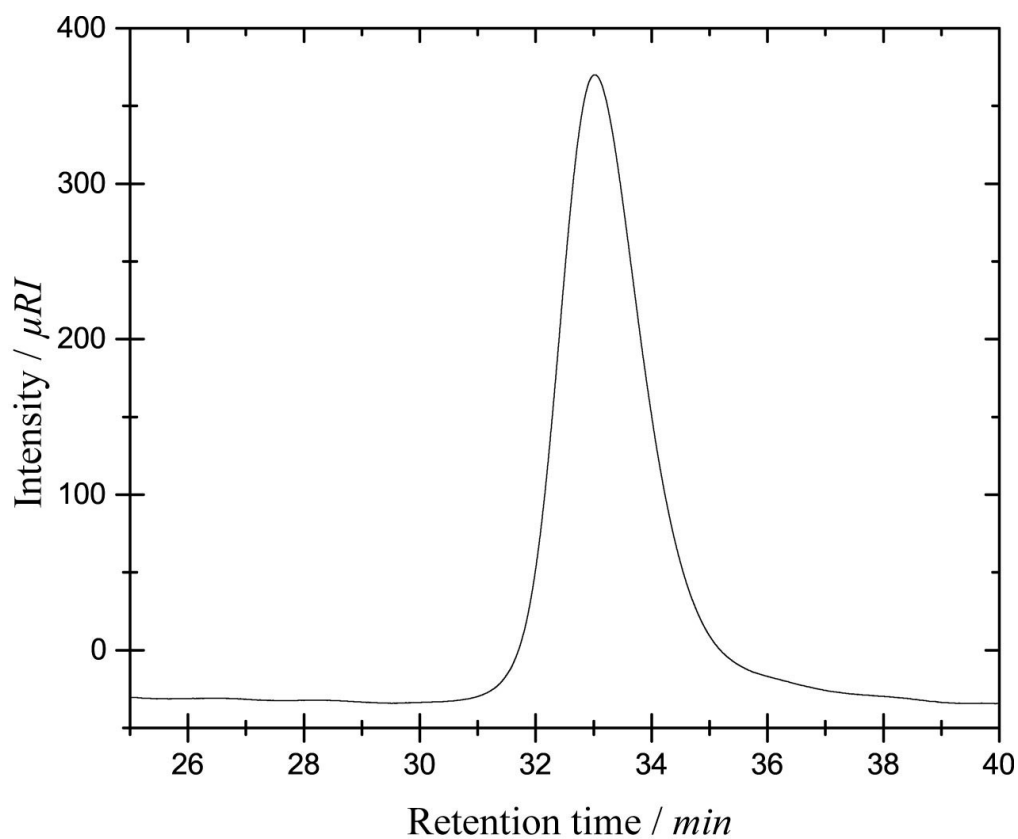


**Figure S12.** SEC traces of  $\alpha$ -(((4,4,5,5-tetramethyl-1,3,2-dioxaborolan-2-yl)benzyl)oxy)- $\omega$ -acetyl

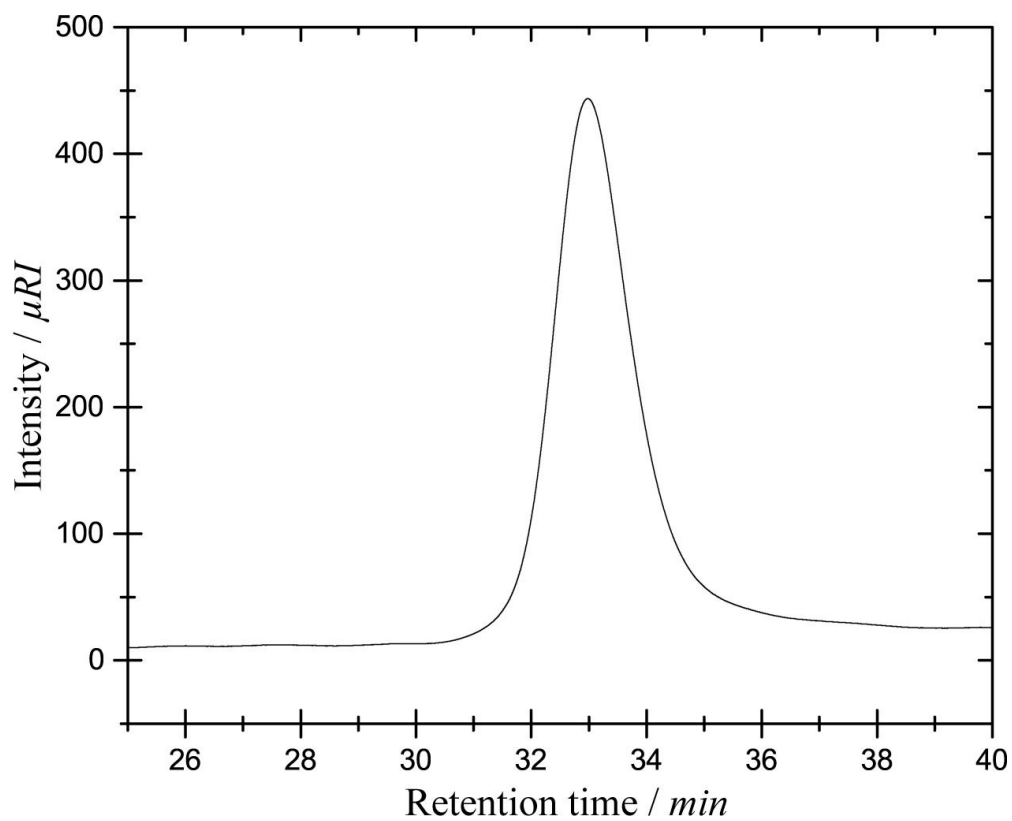


**Figure S13.** SEC traces of  $\alpha$ -((4-boronobenzyl)oxy)- $\omega$ -acetyl polycaprolactone (PCLBA<sub>21</sub>)

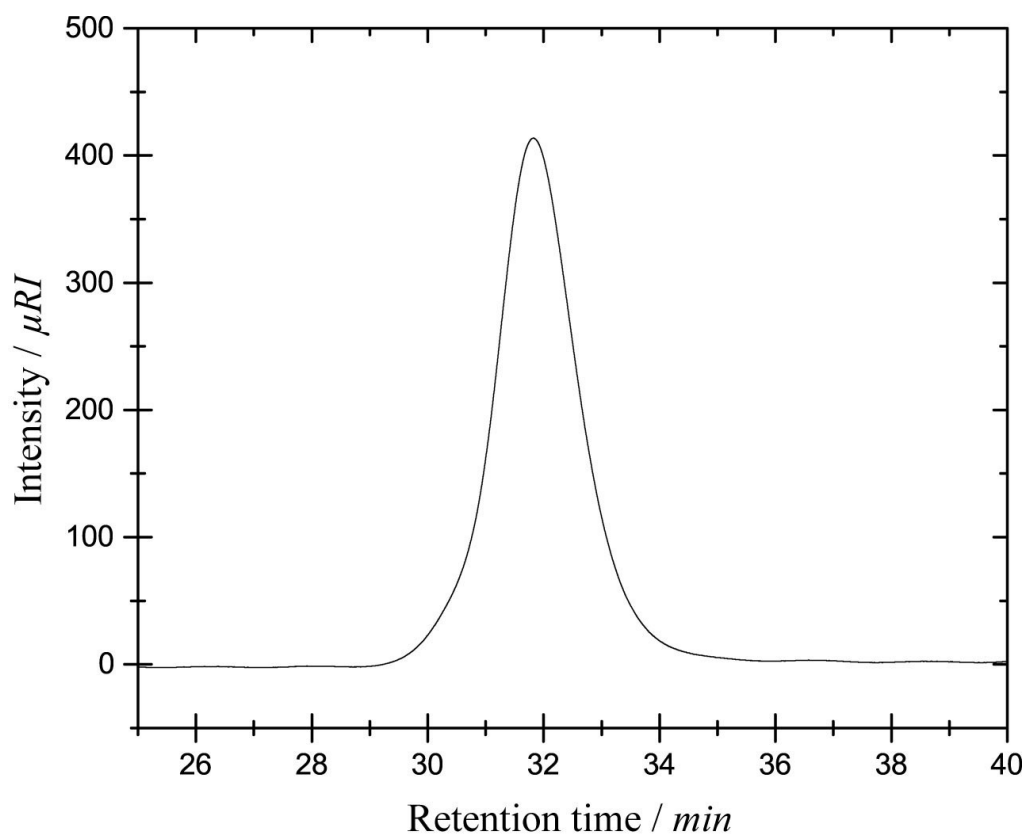


**Figure S14.** SEC traces of  $\alpha$ -(((4,4,5,5-tetramethyl-1,3,2-dioxaborolan-2-yl)benzyl)oxy)polycaprolactone

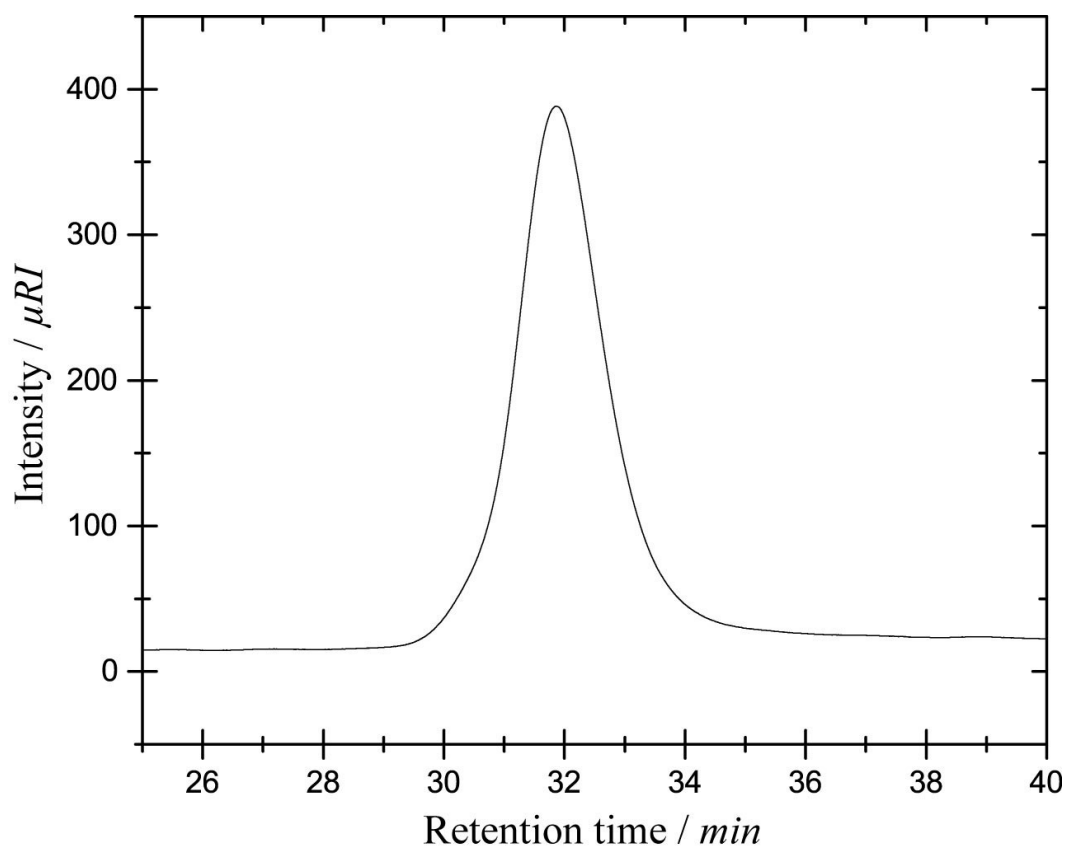


**Figure S15.** SEC traces of  $\alpha$ -(((4,4,5,5-tetramethyl-1,3,2-dioxaborolan-2-yl)benzyl)oxy)- $\omega$ -acetyl

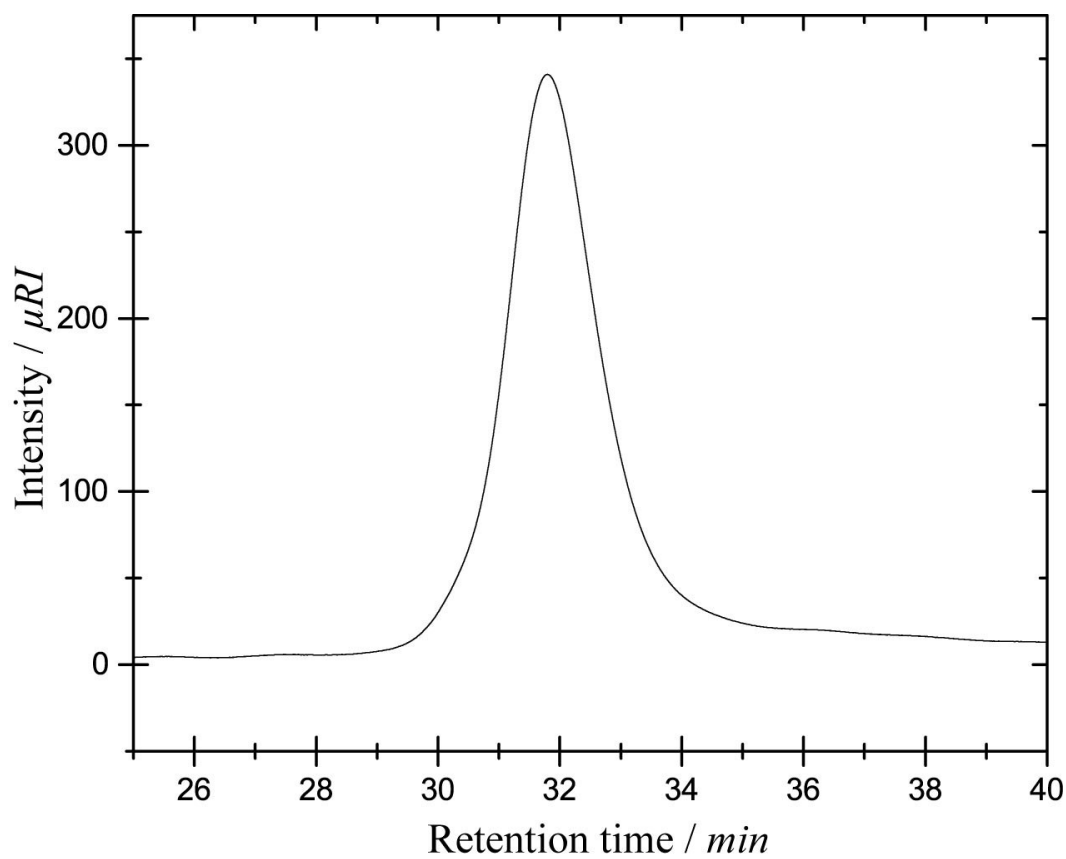


**Figure S16.** SEC traces of  $\alpha$ -((4-boronobenzyl)oxy)- $\omega$ -acetyl polycaprolactone (PCLBA<sub>36</sub>)

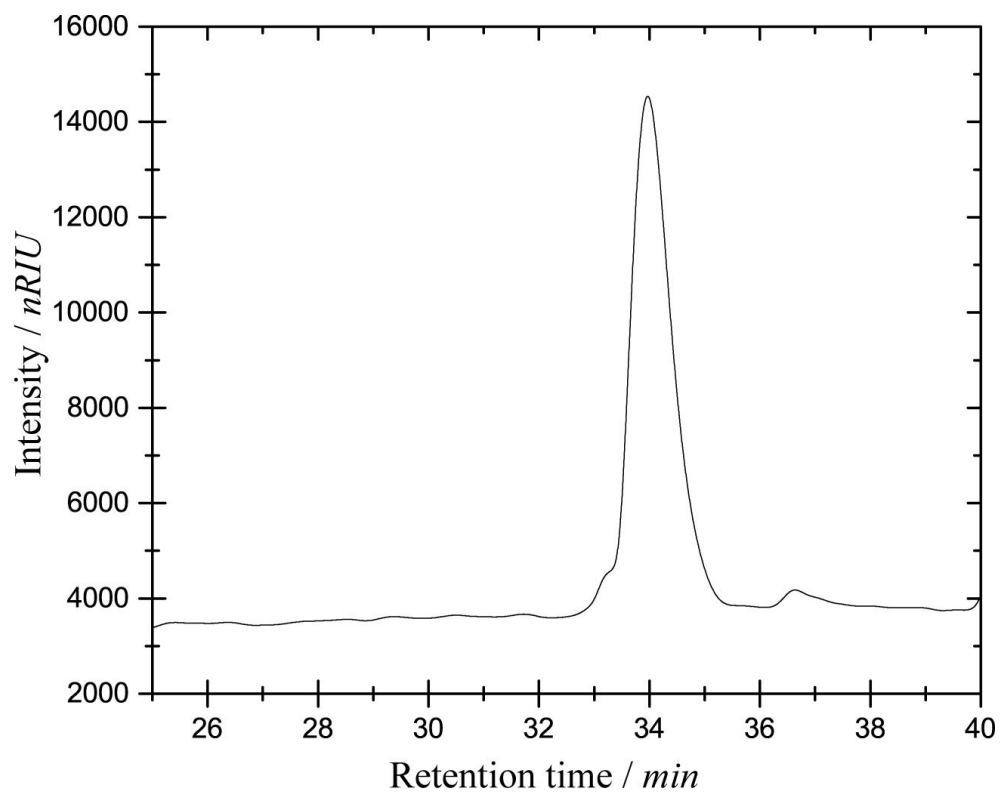


**Figure S17.** SEC traces of  $\alpha$ -methoxy- $\omega$ -propargylpoly(ethylene oxide)

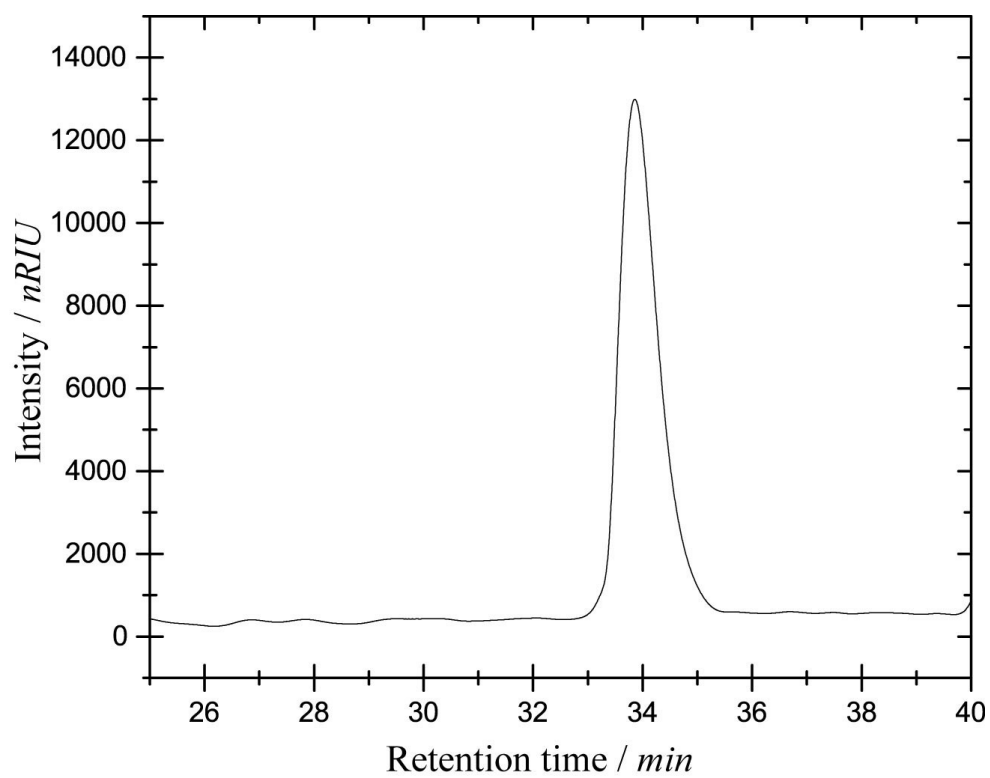


**Figure S18.** SEC traces of  $\alpha$ -methoxy- $\omega$ -propargylpoly(ethylene oxide)

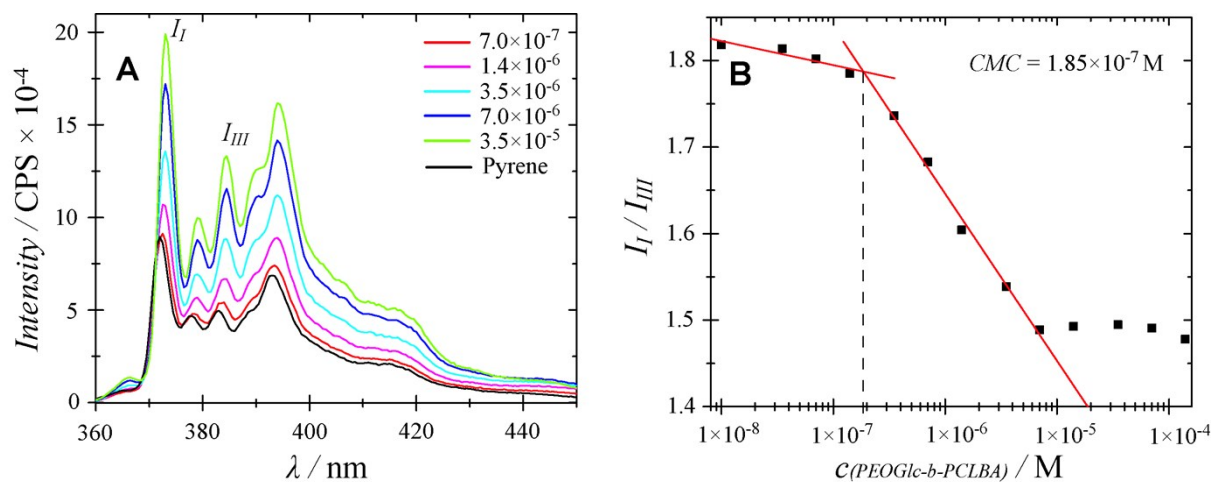


**Figure S19.** (A) Steady-state emission (ex. 336 nm) spectra of pyrene solubilized in aqueous solutions of the PCLBA-*b*-PEOGLc copolymer at different polymer concentrations (as indicated in the figure inset). (B)  $I_I/I_{III}$  ratios as a function of the PCLBA-*b*-PEOGLc copolymer concentration.

In the presence of micelles or other supramolecular aggregates in aqueous solution, pyrene is solubilized in the hydrophobic microphase. Since the spectroscopic properties of pyrene are strongly sensitive to interactions with neighboring molecules, significant changes in both excitation and emission spectra are observed upon formation of micelles and solubilization of pyrene in their hydrophobic cores. Figure S19 (A) shows the changes of pyrene fluorescence emission spectra with increasing copolymer concentration in the solution. The emission spectra were analyzed in the wavelength region of 360–450 nm. At a certain copolymer concentration,  $c = 1.85 \times 10^{-7}$  M, due to a change in pyrene microenvironment, which could be ascribed to the formation of micelles and the corresponding concentration,  $c$ , to the critical micelle concentration, CMC. The first vibronic band  $I_I$  at 372 nm corresponds to a symmetry-forbidden transition, which occurs only due to interactions with surrounding molecules. This effect manifests itself by an increase in the intensity of the fluorescence maximum at 372 nm. The intensity of the third vibronic band  $I_{III}$  at the 383 nm corresponds to a symmetry-allowed transition and hence is not influenced by the microenvironment. The ratio between the intensity of the first and the third vibronic bands of the pyrene emission spectrum,  $I_I / I_{III}$ , decreases with the polarity of the surrounding medium as shown in Figure S19 (B).

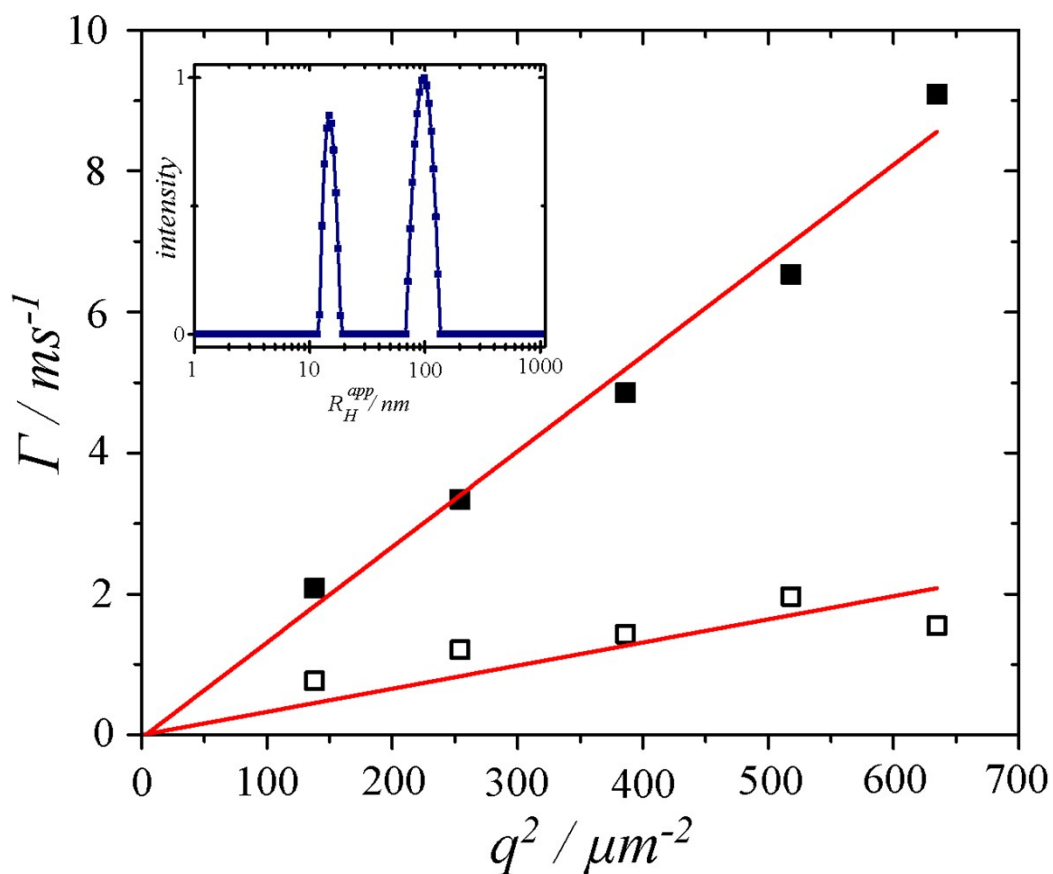


**Figure S20.** Mean relaxation rates of the fast (■) and slow (□) modes of the relaxation time distributions from the DLS measurements of the PCLBA<sub>36</sub>-*b*-PEOGlc<sub>45</sub> nanoparticles as a functions of  $q^2$ . Inset: DLS CONTIN plot (intensity weighted) for PCLBA<sub>36</sub>-*b*-PEOGlc<sub>45</sub> nanoparticles measured at the scattering angle  $\theta = 90^\circ$ .

DLS CONTIN plot, measured at the scattering angle  $\theta = 90^\circ$  for PCLBA<sub>36</sub>-*b*-PEOGlc<sub>45</sub> solution, shows a bimodal distribution of relaxation times (inset of Figure S20). Therefore, we performed the DLS measurements in the angular region  $30^\circ$ - $150^\circ$  to determine whether both observed relaxation modes correspond to diffusive motions. Figure S20 shows the mean relaxation rates,  $\Gamma = \langle \tau \rangle^{-1}$ , calculated from the mean relaxation times of each observed relaxation mode as a function of  $q^2$ . The linear dependences prove that both modes correspond to the diffusion of scattering particles in the solution. The distributions of relaxation times were therefore recalculated to the distributions of apparent hydrodynamic radii,  $R_H^{\text{app}}$

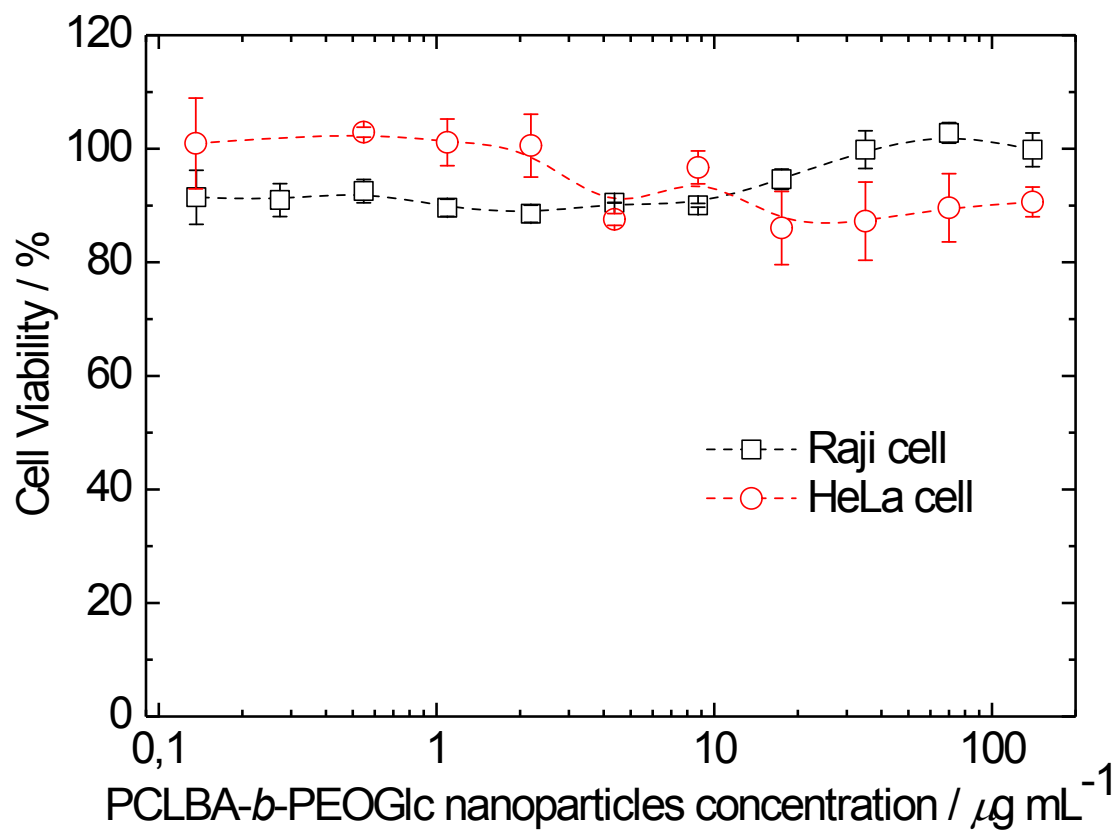


**Figure S21.** Dependence of ( $\square$ ) Raji and ( $\circ$ ) HeLa cells viability on PCLBA-*b*-PEOGlc nanoparticles concentration.